

Regularization by architecture: A deep prior approach for inverse problems

Sören Dittmer^{1,*} · Tobias Kluth^{1,*} · Peter Maass^{1,*} · Daniel Otero Baguer^{1,*}

Received: date / Accepted: date

Abstract The present paper studies the so called deep image prior (DIP) technique in the context of inverse problems. DIP networks have been introduced recently for applications in image processing, [50], also first experimental results for applying DIP to inverse problems have been reported [51]. This paper aims at discussing different interpretations of DIP and to obtain analytic results for specific network designs and linear operators. The main contribution is to introduce the idea of viewing these approaches as the optimization of Tikhonov functionals rather than optimizing networks. Besides theoretical results, we present numerical verifications for an academic example (integration operator) as well as for the inverse problem of magnetic particle imaging (MPI). The reconstructions obtained by deep prior networks are compared with state of the art methods.

Keywords Inverse Problems · Deep Learning · Regularization by Architecture · Deep Inverse Prior · Deep Image Prior

✉ Sören Dittmer
sdittmer@math.uni-bremen.de

Tobias Kluth,
tkluth@math.uni-bremen.de

Peter Maass
pmaass@math.uni-bremen.de

Daniel Otero Baguer
otero@math.uni-bremen.de

¹ Center for Industrial Mathematics (ZeTeM),
University of Bremen, Germany

* Equal contribution

1 Introduction

Deep image priors (DIP) have been recently introduced as a machine learning approach for some tasks in image processing [50]. Usually, such machine learning approaches utilize large sets of training data, hence, it was somewhat surprising that deep image priors are based on a single data point y^δ . The task of DIP is to train a network $\phi_W(z)$ with parameters W by minimizing the simple loss function

$$\|A\phi_W(z) - y^\delta\|^2. \quad (1.1)$$

The minimization is with respect to W , the input z is kept fixed. After training, the solution of the problem is approximated by $\hat{x} = \phi_W(z)$. In image processing typical choices for A are the identity operator (denoising) or a projection operator to a subset of the image domain (inpainting). For these applications it has been observed, that minimizing the functional iteratively by gradient descent methods in combination with a suitable stopping criterion leads to amazing results [50].

This approach is remarkable for several reasons. First of all, the parametrization of a neural network is typically determined during a training phase, afterwards it is fixed and only the input varies in applications. This is based on the assumption, that the set of suitable solutions x to any of the problems mentioned above obeys some probability distribution and that the neural network approach is capable of reproducing this probability distribution by varying the inputs z of a trained network [6]. The DIP approach, however, uses a fixed input and aims at scanning suitable solutions x by varying the parametrization W while z is kept fixed. Secondly, as said above DIP approaches do not use large sets of supervised training data, but rely on a single unsupervised data point. Thirdly, one might assume, that this is only possible, if the network architecture is fine tuned to the specific

task. This is partially true, nevertheless the presented numerical results perform well with somewhat generic network architectures such as autoencoder networks or even general convolutional feedforward networks.

In this paper we are interested in the analysis of DIP approaches and in particular in proving some convergence properties for iteratively minimizing (1.1). We will do so in the context of inverse problems, which are modeled by a non-linear or linear operator $A : X \rightarrow Y$ between Hilbert spaces X and Y . Contrary to the applications in image processing mentioned above, we assume, that the range of A is not closed, which implies, that the inversion or any generalized type of inversion is ill-posed [10, 37, 44]. Typical examples are compact linear operators or parameter-to-state mappings for partial differential equations.

Naive applications of neural networks fail for even the most simple inverse problems, see [38], but there is a growing number of very convincing numerical experiments using suitable network designs for some of the toughest inverse problems such as photo-acoustic tomography [19] or X-ray tomography with very few measurements [2, 20]. Concerning networks based on deep prior approaches for inverse problems, first experimental investigation have been reported, see [50, 51]. Similar as for the above mentioned tasks in image processing, DIP for inverse problems is based on two ingredients:

1. A suitable network design, which leads to our phrase “regularization by architecture”.
2. Training algorithms for iteratively minimizing Expression (1.1) with respect to W in combination with a suitable stopping criterion.

In this paper we present different mathematical interpretations of DIP approaches (Section 2) and we analyze three network designs in the context of inverse problems in more detail.

Our paper is organized as follows. In the next section we discuss some interpretations of DIP approaches and we add a first mathematical result for a trivial network design, which yields a connection to Landweber iterations, which is known to converge for general inverse problems with arbitrary z . Readers solely interested in the mathematical part of the paper may jump directly to Section 3, where we consider a fully connected feed forward network with L identical layers. This leads to the notion of analytic deep prior networks, where one can strictly analyze the convergence properties. The key to the theoretical findings is a change of view, which allows to interpret DIP approaches as optimizing families of Tikhonov functionals. We will exemplify our theoretical finding with numerical examples for the standard linear integration operator (fully connected feed forward network) as well as for the challenging inverse problem posed by magnetic particle imaging (U-Net with skip connections, Section 4).

2 Deep inverse priors and their interpretations

We start with a description of the state of the art of deep image priors before addressing their generalization to inverse problems. In general, a feed forward neural network is an algorithm that starts with an input $x^0 = z$, computes iteratively

$$x^{k+1} = \phi \left(W_k x^k + b_k \right)$$

for $k = 0, \dots, L-1$ and outputs

$$\varphi_W(z) = x^L.$$

The parameters of this system are denoted by

$$W = \{W_0, \dots, W_{L-1}, b_0, \dots, b_{L-1}\}$$

and ϕ denotes a non-linear activation function.

In order to highlight one of the special features of deep image priors, let us first refer to classical generative networks, which e.g. are trained on large sets of “naturally-looking” images. There, W is fixed after training and one expects, that changing the input z will generate different naturally looking images as well [6]. Hence, after training the distribution of naturally looking images is parametrized by z . In contrast to that, deep image priors keep z fixed and aim at parameterizing the distribution of images with W .

In general, this is based on the underlying assumption, that complex distributions, e.g. the distribution of natural images, can be obtained by transforming a simpler distribution. This may be the distribution of the coefficients of a deep network [50] or the coefficients of a wavelet representations, see e.g. [5, 52], moreover it has been argued, that “naturally-looking” images allow a sparse representation in such a basis. In a recent paper that makes use of DIP for compressed sensing [51], the parameter distribution of the network is additionally modeled by some Gaussians that are optimized to fit the distribution of some previously obtained image parametrizations.

To some extend, the success of deep image priors are based on a careful designed network architecture. E.g. [50] used a U-Net-like hourglass architecture with skip connections. In their results they show, that such an architecture can capture the statistics of natural images. However this is still not enough to explain the amazing results they show. In general the DIP learning process may converge towards noisy images or bad reconstructions. The whole success relies on a combination of the network architecture with a suitable stopping rule for the optimization method. The authors of [50] claim that the architecture has an impact on how the solution space is searched during the iterative optimization of the parameters W^* that minimizes (1.1). In their experiments [50] observed that the training process descends quickly to “naturally-looking” images while requiring much

more steps to produce noisy images. Note that this can be somewhat supported by the theoretical findings of [46].

This is also in line with the observations of [55], which shows that deep networks are able to fit noise very well, but need more training time to do so. They consider the CIFAR-10 [34] classification task with different noise models and different common architectures like [48], [35] and a vanilla multilayer perceptron. Another paper that hints in this direction is [3], which analyzes whether neural networks could have a bias towards approximating low frequencies.

2.1 A trivial remark

We now switch to deep priors for solving ill-posed inverse problems. For a given operator A , the general task in inverse problems is to recover an approximation for x^\dagger from measured noisy data

$$y^\delta = Ax^\dagger + \tau,$$

where τ , with $\|\tau\| \leq \delta$, describes the noise in the measurement.

The deep image prior approach to inverse problems asks to train a network $\varphi_W(z)$ with parameters W and fixed input z by minimizing $\|A\varphi_W(z) - y^\delta\|^2$. After training a final run of the network computes $\hat{x} = \varphi_W(z)$ as an approximation to x^\dagger .

We start with an observation for the training process of a trivial network, which simply outputs W , i.e. $\varphi_W(z) = W$. Hence, the approximate solution to the inverse problem is given by $\varphi_W(z) = \hat{x} = W$. Thus W can be identified with an element in X and training this network by gradient descent of $\|A\varphi_W(z) - y^\delta\|^2 = \|AW - y^\delta\|^2$ with respect to W is equivalent to the classical Landweber iteration, which is a gradient descent method for $\|Ax - y^\delta\|^2$ with respect to x .

Despite the obvious trivialization of the neural network approach, this shows that there is potential for training networks with a single data point. Moreover, Landweber iterations converge from rather arbitrary starting points, which indicates that the choice of z in the general case is indeed of minor importance.

2.2 Two Perspectives Based on Regression

In this subsection we present two different perspectives on solving inverse problems with the DIP via the minimization of a functional as discussed in the subsection above. The first perspective is based on a reinterpretation of the minimization of the functional

$$\|A\varphi_W(z) - y^\delta\|^2 \quad (2.1)$$

in the finite, real setting, i.e. $A \in \mathbb{R}^{m \times n}$. This setting lets us write

$$\min_W \|A\varphi_W(z) - y^\delta\|^2 = \min_{x \in \mathcal{R}(\varphi(z))} \|Ax - y^\delta\|^2 \quad (2.2)$$

$$= \min_{x \in \mathcal{R}(\varphi(z))} \sum_{i=1}^m (x^* a_i - y_i^\delta)^2 \quad (2.3)$$

where $\mathcal{R}(\varphi(z))$ denotes the range of the network with regard to W for a fixed z and a_i the rows of the matrix A as well as y_i^δ the entries of the vector y^δ .

This allows for the interpretation that we are solving a linear regression, parameterized by x , which is constrained by a deep learning hypothesis space and given by data pairs of the form (a_i, y_i^δ) .

The second perspective is based on a rewriting of the optimization problem via the method of Lagrange multipliers. We start by considering the constrained optimization problem

$$\min_{x \in X, W} \|Ax - y^\delta\|^2 \text{ s.t. } \|x - \varphi_W(z)\|^2 = 0. \quad (2.4)$$

If we now assume that φ has continuous first partial derivatives with regard to W , the Lagrange functional

$$\mathcal{L}(W, x, \lambda) = \|Ax - y^\delta\|^2 + \lambda \|x - \varphi_W(z)\|^2, \quad (2.5)$$

with the correct Lagrange multiplier $\lambda = \lambda_0$, has a stationary point at each minimum of the original constraint optimization problem. This gives us a direct connection to unconstrained variational approaches like Tikhonov functionals.

2.3 The Bayesian point of view

The Bayesian approach to inverse problems focuses on computing MAP (maximum a posteriori probability) estimators, i.e. one aims for

$$\hat{x} = \arg \max_{x \in X} p(x|y^\delta), \quad (2.6)$$

where $p : X \times Y \rightarrow \mathbb{R}$ is a conditional PDF. From standard Bayesian theory we obtain

$$\hat{x} = \arg \min_{x \in X} \left\{ -\log[p(y^\delta|x)] - \log[p(x)] \right\}. \quad (2.7)$$

The setting for inverse problems, i.e. $Ax + \tau = y^\delta$ with $\tau \sim \mathcal{N}(0, \sigma^2 \mathbb{1}_Y)$, yields $(\lambda = 2\sigma^2)$

$$\hat{x} =: \arg \min_{x \in X} \|Ax - y^\delta\|^2 - \lambda \log[p(x)].$$

We now decompose x into $x_\perp := P_{\mathcal{N}(A)^\perp}(x)$, and $x_{\mathcal{N}} := P_{\mathcal{N}(A)}(x)$, where $P_{\mathcal{N}(A)}(x)$, resp. $P_{\mathcal{N}(A)^\perp}(x)$, denotes the orthogonal projection onto $\mathcal{N}(A)$, resp. $\mathcal{N}(A)^\perp$. Setting $\hat{x} =$

$(x_{\mathcal{N}}, x_{\perp})$ yields

$$\begin{aligned} \hat{x} &= \arg \min_{x \in X} \|Ax_{\perp} - y^{\delta}\|^2 - \lambda \log p(x_{\mathcal{N}}, x_{\perp}) \\ &= \arg \min_{x \in X} \|Ax_{\perp} - y^{\delta}\|^2 - \lambda \log p(x_{\perp}) - \lambda \log p(x_{\mathcal{N}}|x_{\perp}). \\ &= \arg \min_{x \in X} \underbrace{\|Ax_{\perp} - y^{\delta}\|^2}_{(I)} - \underbrace{\lambda \log p(x_{\perp}) - \lambda \log p(x_{\mathcal{N}}|x_{\perp})}_{(II)}. \end{aligned}$$

The data y^{δ} only contains information about x_{\perp} , which in classical regularization is exploited by restricting any reconstruction to $\mathcal{N}(A)^{\perp}$.

However, if available, $p(x_{\mathcal{N}}|x_{\perp})$ is a measure on how to extend x_{\perp} with an $x_{\perp} \in \mathcal{N}(A)^{\perp}$ to a suitable $x = (x_{\mathcal{N}}, x_{\perp})$. The classical regularization of inverse problems simply uses an extension by zero, i.e. $x = (0, x_{\perp})$, which not necessarily is optimal. If we accept the interpretation that a network can be a meaningful parametrization of the set of suitable solutions x , then $p(x) \equiv 0$ for all x not in the range of the network and optimizing the network will indeed yield a non-trivial completion $x = (x_{\mathcal{N}}, x_{\perp})$. More precisely (I) can be interpreted to be a deep prior on the measurement and (II) to be a deep prior on the nullspace part of the problem.

3 Deep inverse priors and Tikhonov functionals

3.1 A general setting for deep priors for inverse problems

In this section we consider linear operators A and aim at rephrasing DIP, i.e. the minimization of (1.1) with respect to W , as an approach for learning optimized Tikhonov functionals. This change of view, i.e. regarding deep inverse priors as an optimization of functionals rather than networks, opens the way for analytic investigations.

We now follow the well known approach of LISTA [15] (learned iterated soft thresholding algorithm) or learned PG (proximal gradient) methods as stated in Appendix I. Note, that our loss function is identical with the loss functions used in LISTA or learned PG methods, but using only a single data point. More precisely, we use the particular architecture of a fully connected feedforward network with L layers of identical size defined by

$$\varphi_W(z) = x^L, \quad (3.1)$$

where

$$x^{k+1} = \phi(Wx^k + b) \quad (3.2)$$

for $k = 0, \dots, L-1$ and $x^0 = z$.

I.e. the affine linear map given by (W, b) is the same for all layers. Moreover the activation function of the network is chosen as the proximal mapping of a regularizing functional

$\lambda \alpha R$, we restrict the matrix W by enforcing $I - W = \lambda B^* B$ (I denotes the identity operator) for some B and the bias is determined via $b = \lambda B^* y^{\delta}$.

Remark 3.1 This kind of generalized ISTA or PG schemes converge for rather arbitrary starting points, i.e. the particular choice of z in the deep prior context indeed is of minor importance.

Remark 3.2 Restricting activation functions to be proximal mappings is not as severe as it might look at first glance. E.g. ReLU is the proximal mapping for the indicator function of positive real numbers and soft shrinkage is the proximal mapping for the modulus function.

In this setting, the output $\varphi_W(z)$ of the network is identical to the L -th iterate of a proximal gradient descent method for minimizing

$$J_B(x) = \frac{1}{2} \|Bx - y^{\delta}\|^2 + \alpha R(x), \quad (3.3)$$

see Appendix I. Hence, updating B or W changes the discrepancy term in this Tikhonov functional.

In this section we neglect the difference between $\varphi_W(z)$ and $x(B) = \arg \min J_B(x)$ and assume that the PG scheme has fully converged, i.e.

$$\varphi_W(z) = \arg \min J_B(x). \quad (3.4)$$

This leads to the definition of analytic deep priors.

Definition 3.1 Consider a fully connected neural network φ_W with L layers, whose activation function is a proximal mapping $\text{Prox}_{\alpha \lambda R}$ with respect to a convex functional $R : X \rightarrow \mathbb{R}$, i.e.

$$\varphi_W(z) = x^L, \quad (3.5)$$

where

$$x^{k+1} = \text{Prox}_{\alpha \lambda R}(Wx^k + b) \quad (3.6)$$

and $x_0 = z$. Further assume that W can be decomposed as $W = I - B^* B$ with a bounded operator $B : X \rightarrow W$ and that the bias satisfies $b = \lambda B^* y^{\delta}$. We define the associated Tikhonov functional $J_B(x) = \frac{1}{2} \|Bx - y^{\delta}\|^2 + \alpha R(x)$ and assume that a unique minimizer $x(B) = \arg \min J_B(x)$ exists. We call this setting an analytic deep prior if W , resp. B , is trained from a single data point y^{δ} by gradient descent applied to

$$\min_B \|Ax(B) - y^{\delta}\|^2. \quad (3.7)$$

We now examine the training process for computing W , resp. B , in the setting of such analytic deep prior models. This can be either regarded as training a neural network or as determining an optimized Tikhonov functional. In the following we focus on the minimization with respect to B and

then set $W = I - \lambda B^* B$, which yields a more convenient notation. Hence, the training of the network for given data y^δ is achieved by a gradient descent method with respect to B for the loss function

$$F(B) = \frac{1}{2} \|Ax(B) - y^\delta\|^2 \quad \text{s.t. } x(B) = \arg \min_x J_B(x). \quad (3.8)$$

The stationary points are characterized by $\partial F(B) = 0$ and gradient descent iterations with stepsize η are given by

$$B^{\ell+1} = B^\ell - \eta \partial F(B^\ell). \quad (3.9)$$

Hence we need to compute the derivative of F with respect to B .

Lemma 3.1 *Consider an analytic deep prior network. We define*

$$x(B) = \arg \min J_B(x), \quad (3.10)$$

$$\psi(x, B) = \text{Prox}_{\lambda \alpha R} \left(x - \lambda B^* (Bx - y^\delta) \right) - x. \quad (3.11)$$

Then

$$\partial F(B) = \partial x(B)^* A^* (Ax(B) - y^\delta) \quad (3.12)$$

with

$$\partial x(B) = -\psi_x(x(B), B)^{-1} \psi_B(x(B), B), \quad (3.13)$$

which leads to the gradient descent

$$B^{\ell+1} = B^\ell - \eta \partial F(B^\ell). \quad (3.14)$$

Proof F is a functional which maps operators B to real numbers, hence, its derivative is given by

$$\partial F(B) = \partial x(B)^* A^* (Ax(B) - y^\delta),$$

which follows from classical variational calculus, see e.g. [10].

The derivative of $x(B) = \arg \min J_B(x)$ with respect to B can be computed using the fix point condition for a minimizer of J_B :

$$\text{Prox}_{\lambda \alpha R} \left(x(B) - \lambda B^* (Bx - y^\delta) \right) - x(B) = 0,$$

which is equivalent to

$$\psi(x(B), B) = 0.$$

We apply implicit function theorem applied and obtain the derivative $\partial x(B)$

$$\partial x(B) = -\psi_x(x(B), B)^{-1} \psi_B(x(B), B).$$

Combining $\partial F(B)$ with $\partial x(B)$ yields the required result. \square

This lemma allows to obtain an explicit description of the gradient descent for W or B , which in turn leads to an iteration of functionals J_B and minimizers $x(B)$. We will now exemplify this derivation for a rather academic example, which however highlights in particular the differences between a classical Tikhonov minimizer, i.e.

$$x_T = \arg \min J_A(x) = \arg \min \frac{1}{2} \|Ax - y^\delta\|^2 + \alpha R(x),$$

and the solution of the DIP approach.

3.1.1 Example

In this example we examine analytic deep priors for linear inverse problems $A : X \rightarrow Y$, i.e. $A, B \in \mathcal{L}(X, Y)$, and

$$R(x) = \frac{1}{2} \|x\|^2. \quad (3.15)$$

The rather abstract characterization of the previous section can be made explicit for this setting. We consider the classical Tikhonov regularization, i.e.

$$x_T = (A^*A + \alpha I)^{-1} A^* y^\delta. \quad (3.16)$$

This is equivalent to the solution obtained by the analytic deep prior approach with $B = A$ without any iteration. We then take $B^0 = A$ as a starting point. First of all we compute one step of gradient descent for minimizing (1.1) with respect to B and see, how the the resulting $x(B)$ differs from x_T .

The proximal mapping corresponding to the functional R above is given by

$$\text{Prox}_{\lambda \alpha R}(z) = \frac{1}{1 + \lambda \alpha} z. \quad (3.17)$$

We use the explicit description of the iteration

$$B^{\ell+1} = B^\ell - \eta \partial F(B^\ell) \quad (3.18)$$

with

$$\partial F(B) = \partial x(B)^* A^* (Ax(B) - y^\delta) \quad (3.19)$$

In this case $x(B)$, which is a mapping $x : \mathcal{L}(X, Y) \rightarrow X$, can be compute explicitly as

$$x(B) = \arg \min J_B(x) = (B^*B + \alpha I)^{-1} B^* y^\delta. \quad (3.20)$$

The derivative of $x(B)$ with respect to B is a linear map $\partial x(B) : \mathcal{L}(X, Y) \rightarrow X$. For $\delta B \in \mathcal{L}(X, Y)$ we obtain

$$\begin{aligned} \partial x(B)(\delta B) = & - (B^*B + \alpha I)^{-2} (\delta B^*B + B^*\delta B) B^* y^\delta \\ & + (B^*B + \alpha I)^{-1} \delta B^* y^\delta. \end{aligned} \quad (3.21)$$

The adjoint operator is a mapping from X to $\mathcal{L}(X, Y)$, which can be derived from the defining relation

$$\langle \partial x(B)(\delta B), z \rangle_X = \langle \delta B, [\partial x(B)]^* z \rangle_{\mathcal{L}(X, Y)}. \quad (3.22)$$

Hence,

$$\begin{aligned} [\partial x(B)]^* z = & -BB^*y^\delta z^*(B^*B + \alpha I)^{-2} \\ & - B(B^*B + \alpha I)^{-2}z(y^\delta)^*B \\ & + y^\delta z^*(B^*B + \alpha I)^{-1}. \end{aligned} \quad (3.23)$$

Here, $y^\delta z^* \in \mathcal{L}(X, Y)$ denotes a linear map, which maps an $x \in X$ to $\langle z, x \rangle_X y^\delta$.

First of all, we now aim at determining explicitly

$$\partial F(B) = \partial x(B)^* A^* (Ax(B) - y^\delta) \quad (3.24)$$

at the starting point of our iteration, i.e. with $B^0 = A$. I.e. we initialize the iteration with $x(A)$, where $x(A) = (A^*A + \alpha I)^{-1}A^*y^\delta$ is the classical Tikhonov regularization. Inserting this yields

$$A^*(Ax(A) - y^\delta) = -\alpha(A^*A + \alpha I)^{-1}A^*y^\delta. \quad (3.25)$$

From this follows a rather lengthy expression for

$$\partial F(A) = \partial x(A)^* A^* (Ax(A) - y^\delta) \quad (3.26)$$

$$\begin{aligned} & = \alpha AA^*y^\delta (y^\delta)^* A(A^*A + \alpha I)^{-3} \\ & + \alpha A(A^*A + \alpha I)^{-3}A^*y^\delta (y^\delta)^* A \\ & - \alpha y^\delta (y^\delta)^* A(A^*A + \alpha I)^{-2}. \end{aligned} \quad (3.27)$$

and we can compute the update

$$B_1 = A - \eta \partial F(A) \quad (3.28)$$

as well as the output of the analytic deep prior approach after one iteration of updating B (assuming a suitably chosen η)

$$x(B_1) = (B_1^*B_1 + \alpha I)^{-1}B_1^*y^\delta. \quad (3.29)$$

This expression nicely collapses if $y^\delta (y^\delta)^*$ commutes with AA^* . For illustration we assume the rather unrealistic case that $x^\dagger = u$, where u is a singular function for A with singular value σ . The dual singular function is denoted by v , i.e. $Au = \sigma v$ and $A^*v = \sigma u$ and we further assume, that the measurement noise in y^δ is in the direction of this singular function, i.e. $y^\delta = (\sigma + \delta)v$. In this case, the problem is indeed one-dimensional and we obtain an iteration restricted to the span of u , resp. the span of v .

A lengthy computation exploiting $B^0 = A$ and $\beta_0 = \sigma$ shows that the singular value β_ℓ of u in the spectral decomposition of B^ℓ obeys the iteration

$$\beta_{\ell+1} = \beta_\ell - \eta \sigma (\sigma + \delta)^2 (\alpha + \beta_\ell^2 - \sigma \beta_\ell) \frac{\beta_\ell^2 - \alpha}{(\beta_\ell^2 + \alpha)^3},$$

i.e.

$$B^{\ell+1} = B^\ell - c_\ell v u^* \quad (3.30)$$

with

$$c_\ell = c(\alpha, \delta, \sigma, \eta) = \eta \sigma (\sigma + \delta)^2 (\alpha + \beta_\ell^2 - \sigma \beta_\ell) \frac{\beta_\ell^2 - \alpha}{(\beta_\ell^2 + \alpha)^3}.$$

This iteration has a contracting fix point at $\beta = \sqrt{\alpha}$, which yields

$$x(B) = \frac{1}{2\sqrt{\alpha}} (\sigma + \delta) u$$

as opposed to the Tikhonov minimizer $x_T = \frac{\sigma}{\sigma^2 + \alpha} (\sigma + \delta) u$.

For fixed α , our value $\beta = \frac{1}{2\sqrt{\alpha}}$ is the maximum of $\frac{\sigma}{\sigma^2 + \alpha}$ for varying σ . Our artificial setting is one-dimensional and hence well-posed, i.e. we do not want to regularize or diminish the reconstruction. In this sense, DIP iterations converge to the optimal value for Tikhonov type regularizers for this one-dimensional case.

3.2 Some numerical experiments

We now use the analytic deep inverse prior approach for solving an inverse problem with the following integration operator $A : L^2([0, 1]) \rightarrow L^2([0, 1])$

$$(Ax)(t) = \int_0^t x(s) ds. \quad (3.31)$$

A is linear and compact, hence the inverse problem is ill-posed. We let the matrix $A_n \in \mathbb{R}^{n \times n}$ be a discretization of A and choose $x^\dagger \in \mathbb{R}^n$ to be one of its singular vectors u . Then we set the noisy data $y^\delta = A_n x^\dagger + \tau$ with $\tau \sim \mathcal{N}(0, \sigma^2 \mathbb{1}_n)$ and σ equals 10% of the largest coefficient of y^\dagger , see Figure 3.1.

We aim to recover x^\dagger from y^δ considering the setting established in Def. 3.1 for $R(\cdot) = \frac{1}{2} \|\cdot\|^2$ and a fixed value of α . That means the solution x is parametrized by the weight matrix B of the network, i.e. $x(B) = \varphi_W(z)$ with $W = I - B^T B$ and $z \in \mathbb{R}^n$ some arbitrary fixed input. Solving the inverse problem is now equivalent to training the network $\varphi_W(z)$, i.e. finding optimal B , to minimize the loss function (1.1) for the single data point (z, y^δ) . Afterwards, the reconstruction is obtained by computing $x(B) = \arg \min J_B$.

In order to properly update B by back-propagation, the network was implemented taking special care ensuring that (3.4) holds. For more details please refer to Appendix II.

In Figure 3.2 some reconstruction results are shown. The first plot contains the true solution x^\dagger , the standard Tikhonov solution x_T , and the reconstruction obtained with the analytic deep inverse approach $x(B_{opt})$ after B seemed to have converged, in this case that means B_{opt} is the resulting matrix after 4000 training iterations. Figure 3.2 provides some additional reconstructions and plots depicting:

- The true error of the network's output $x(B)$ after each update of B in a logarithmic scale.

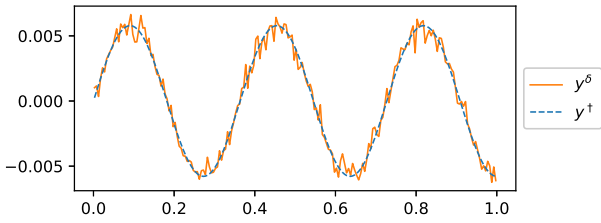


Fig. 3.1 Example of y^δ for $x^\dagger = u_5$ and 10% of noise.

- The Frobenius norm of $A - B$ after each update of B .
- The matrix B_{opt} .

For all choices of α the training of B converges to a matrix B_{opt} , such that $x(B_{opt})$ has a smaller true error than x_T . As it can be observed in the last plot, B_{opt} contains some patterns that reflect what was previously obtained in Equation 3.30. The analytic deep inverse prior approach seems in principle to behave differently than the Tikhonov approach and shows some promising results.

So far, we considered the regularization parameter α to be fixed. In a real application one needs to choose it by a technique such as the L-curve [18] or the discrepancy principle. However, they usually involve finding reconstructions for many different values of α . In our case, that would mean to retrain the network each time, which would amount to high computational costs. This motivates an adaptive choice of α during the optimization, which could be achieved by letting α to be also a trainable weight of the network. The results for the same example and different starting values α_0 are shown in Figure 3.3.

Since we are minimizing (1.1), it becomes now important to choose when to stop the training, otherwise α will probably converge to 0 and B will converge to A , which would result in bad reconstructions. We did that by monitoring the trajectory/change of α over the course of the training. We stopped at an iteration k^* , chosen to be close to the corner of the trajectory depicted in Figure 3.3, i.e. when α starts decreasing very slow. We discuss this further in Appendix II.

4 Deep priors for magnetic particle imaging

In the remainder of this paper we apply a deep inverse prior network for solving the reconstruction problem in magnetic particle imaging (MPI). MPI is an imaging modality based on injecting ferromagnetic nanoparticles, which are consequently transported by the blood flow. Reconstructing the resulting spatial distribution $c(x)$ of those nanoparticles is based on exploiting the nonlinear magnetization behavior of ferromagnetic nanoparticles [14].

More precisely, one applies a magnetic field, which is a superposition of a static gradient field, which generates a

field-free-point (FFP), and a highly dynamic spatially homogeneous field, which moves the FFP in space. The mean magnetic moment of the nanoparticles in the neighborhood of the FFP will generate an electro-magnetic field, whose voltages can be measured by so-called receive coils. The time-dependent measurements $v_\ell(t)$ in the receive coils constitute the data for the inversion process, i.e. for reconstructing $c(x)$.

MPI benefits from a high temporal resolution and a potentially high spatial resolution which makes it suitable for several *in-vivo* applications, such as imaging blood flow [21, 53], instrument tracking [16] and guidance [45], flow estimation [13], cancer detection [54] and treatment by hyperthermia [41].

Due to the nonmagnetic coating of the nanoparticles, which largely suppresses particle-particle interactions, MPI is usually modeled by a linear Fredholm integral equation of the first kind describing the relationship between particle concentration and the measured voltage. After removing the voltage induced by the applied magnetic field one obtains a measured signal from the ℓ -th receive coil as

$$v_\ell(t)^\delta = v_\ell(t) + \tau$$

where

$$v_\ell(t) = S_\ell c(t) := \int_{\Omega} c(x) s_\ell(x, t) dt,$$

τ , with $\|\tau\| \leq \delta$, some noise and s_ℓ the kernel of the linear operator. Combining the measurements of all receive coils yields – after discretization and applying the Fourier transform – a linear system of equations $Sc = v^\delta$. Typically, the rows of S are normalized resulting in the final form of the linearized inverse problem denoted by

$$Ac = y^\delta. \quad (4.1)$$

This is a coarse simplification of the physical setup, which neglects non-linear magnetization effects of the nanoparticles as well as the non-homogeneity of the spatial sensitivity of the receive coils and also the small, but non-negligible particle-particle interactions. Hence, this is a perfect setup for exploiting the potential of neural networks for matching complex and high-dimensional non-linear models.

For a more detailed introduction to MPI, details on data preprocessing as well as on the implementation using Tensorflow [1], see Appendix III. In this section we just report some numerical results.

We test the capability of the Deep Imaging Prior approach to improve image reconstruction obtained by standard Tikhonov regularization. For the experiments we use the datasets (D1) and in the Appendix III also (D2) generated by the Bruker preclinical MPI system at the University Medical Center Hamburg-Eppendorf, see Appendix III. We

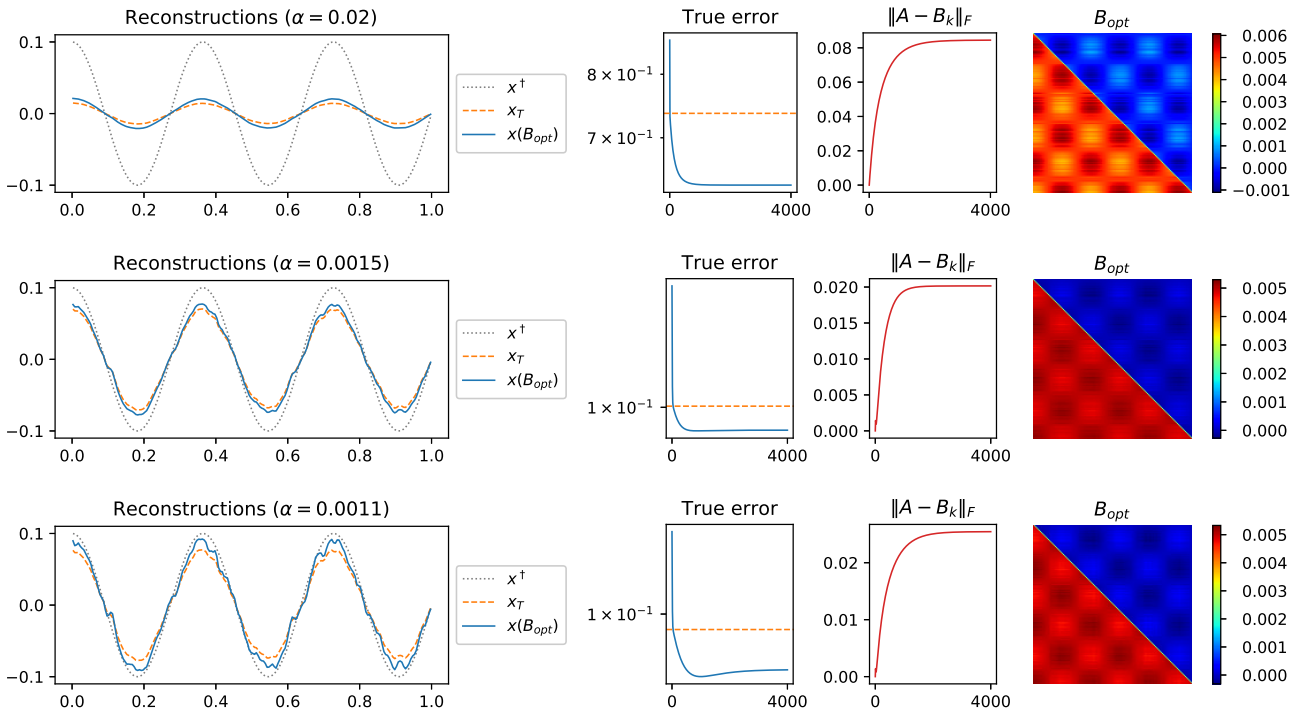


Fig. 3.2 Reconstructions for different fixed values of α . The broken line in the second plot indicates the true error of the standard Tikhonov solution x_T . In the third plot one can check that B indeed converges to some matrix B_{opt} , which is shown in the last plot. The networks were trained with the standard gradient descent method and a learning rate of 0.05. In all cases 4000 training iterations are shown.

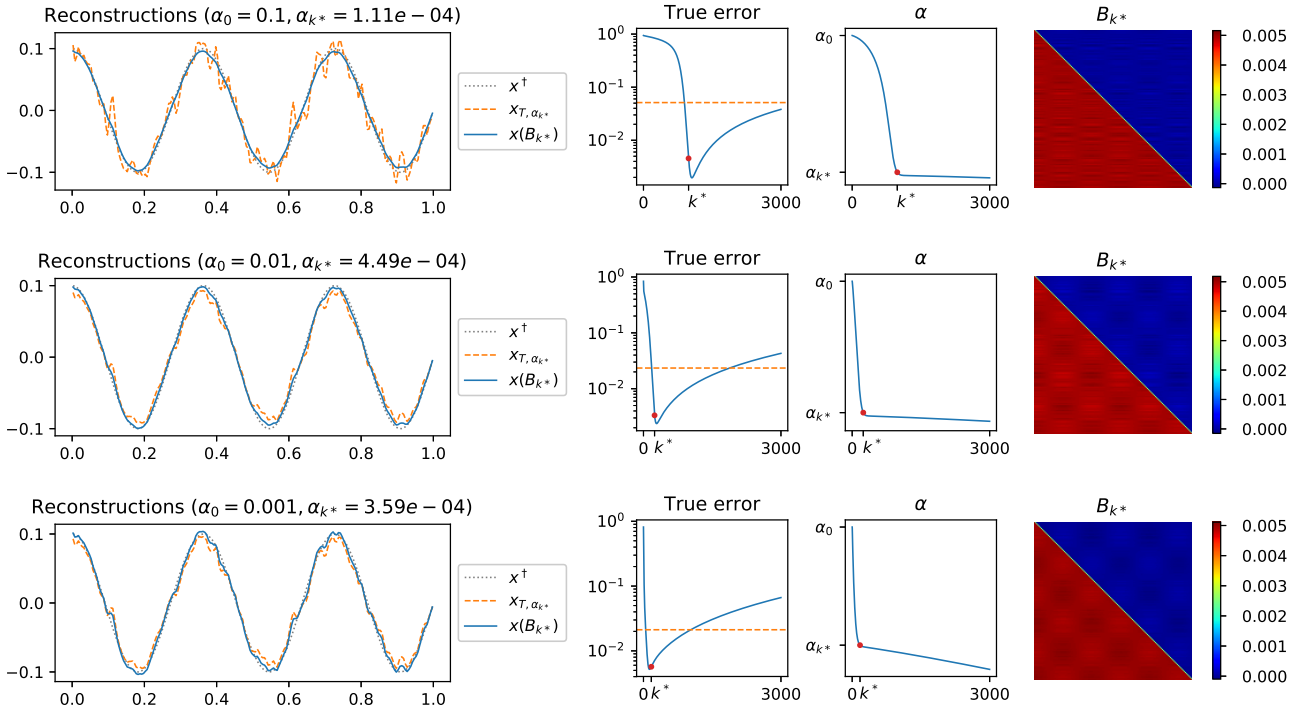


Fig. 3.3 Reconstructions with an adaptive α for different starting values α_0 . The dot indicates the selected iteration k^* . The broken line in the second plot indicates the true error of the standard Tikhonov solution $x_{T, \alpha_{k^*}}$ for $\alpha = \alpha_{k^*}$. The networks were trained with gradient descent using 0.1 as learning rate and in all the cases 3000 iterations are shown.

use the deep image prior network introduced by [50], specifically their U-net architecture. For further details on this architecture we refer to Appendix III and [50].

The measured voltages are given as a sequence of complex numbers, hence we split up our **loss function** into the form

$$\|A\phi_W(z) - y^\delta\|^2 = \|\operatorname{Re}(A)\phi_W(z) - \operatorname{Re}(y^\delta)\|^2 \quad (4.2)$$

$$+ \|\operatorname{Im}(A)\phi_W(z) - \operatorname{Im}(y^\delta)\|^2, \quad (4.3)$$

where Re and Im denote the real and imaginary parts respectively.

For comparison to our deep inverse prior MPI reconstructions, we also compute sparse and classical Tikhonov reconstructions. We produce the Tikhonov reconstruction, usually associated with the minimization of the functional

$$\|Ac - y^\delta\|^2 + \lambda \|c\|^2, \quad (4.4)$$

via the algebraic reconstruction technique (Kaczmarz) as generalized to allow for the constraint $c \geq 0$ by [9]. We produce the sparsity reconstruction, usually associated with the minimization of the functional

$$\|Ac - y^\delta\|^2 + \lambda \|c\|_1, \quad (4.5)$$

via simply implementing this functional in Tensorflow and minimizing it via gradient descent. In the end we project each entry into $\mathbb{R}_{\geq 0}$.

We start by presenting direct comparisons of the Kaczmarz, sparsity and DIP reconstructions in Table 4.1. Beneath each image we state the parameters we used for the reconstruction $\tilde{\lambda} = \|A\|_F^2 \lambda$, where $\|\cdot\|_F$ denotes the Frobenius norm and λ is the regularization parameter as used in Equations 4.4 or 4.5 and η the learning rate used for Adam. For DIP we always used early stopping after 1000 optimization steps. The images started to deteriorate slowly for more iterations.

As one can see, the results presented in Table 4.1 are roughly on par with, if not even better than, the classical regularization methods. In particular we want to point out the reconstruction of the “2mm” phantom for which only the DIP approach achieves a separation of the two different lines.

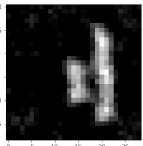
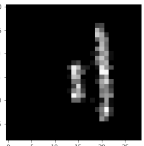
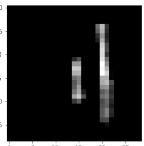
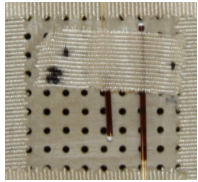
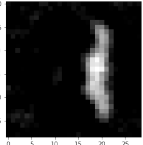
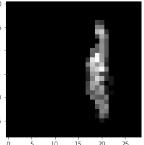
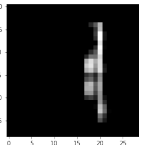
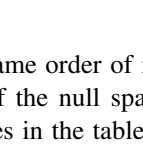
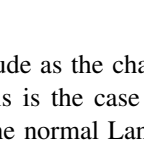
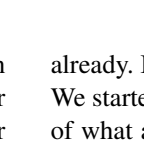
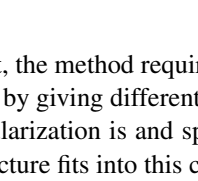
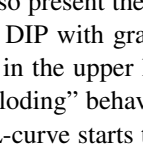
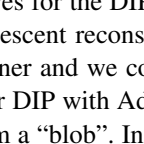
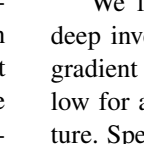
We now want to compare the DIP based reconstruction process with a Landweber reconstruction with early stopping in more detail. Here we use a phantom in the shape of a “one” provided in DS1. Specifically we compare a DIP reconstruction obtained with Adam [22] with a DIP reconstruction obtained with gradient descent and with the previously mentioned Landweber reconstruction, see Table 4.2. To compare them we present the following quantities:

1. **Error:** The quantity we are minimizing over the iterations of the optimization. I.e. $\|Ac_t - y^\delta\|^2$ (y-axis) over t (x-axis), where t is the iteration index and c_t the reconstruction at iteration t .
2. **L-curve:** The path of the points $(\|Ac_t - y^\delta\|^2, \|c_t\|^2)$ over t , where $\|Ac_t - y^\delta\|^2$ is on the x-axis and $\|c_t\|^2$ on the y-axis. Note that these paths tend to start in the bottom right corner and moves gradually towards the upper left corner.
3. **Change:** The change in c_t that happens over the course of the optimization, separately displayed for the spaces $\mathcal{N}(A)$ and $\mathcal{N}(A)^\perp$. I.e. we plot $\|P_{\mathcal{N}(A)}(c_t - c_{t-1})\|^2$ (y-axis) and $\|P_{\mathcal{N}(A)^\perp}(c_t - c_{t-1})\|^2$ (y-axis) over t (x-axis). Here P_X denotes the orthogonal projection onto the space X .
4. **Errors per Singular Value:** For each t we plot the normalized errors associated with each of the one-dimensional linear subspaces spanned by the singular vectors, ordered by the size of their associated singular values, starting with the biggest singular value at 0. I.e. for the singular value decomposition $A = U\Sigma V^*$ of A , where Σ a ordered diagonal matrix and U and V orthogonal, we plot the quantity $(V^*c_t - U^*y^\delta)_i^2$ over the index t and the index i .
5. **Final Reconstruction:** The reconstruction at the end of the optimization, i.e. c_T , where T the total number of iterations.

First of all we would like to point out that for the plain Landweber reconstruction and the Adam DIP reconstruction we used 500 optimization steps each, but for the gradient descent DIP reconstruction we needed 200 times that many steps, i.e. 100,000 steps, to get a reconstruction that did not seem to improve anymore. Also the best Adam reconstruction, based on our visual judgment, was not the final one. The best one was reached after approximately 100 iterations. For both DIP reconstructions we used a learning rate of $5e-5$ and for Landweber we chose $1e-2$, since the result did not seem to change much based on the learning rate. If we look at the best reconstructions, we can see that both DIP reconstructions look quite good, although the gradient descent one displays the gap between the two dashes of the “one”. The reason we did not use gradient descent instead of Adam for all our reconstructions is first, that one needs to use small learning rates with gradient descent to get good reconstructions and therefore, as already mentioned, one needs considerably more steps to reach good results. Second, the optimization process does not only take much longer than the one with Adam, but also seems to get stuck in bad local minima most of the time.

As one can see the error curves of the three different methods displayed in Table 4.2 look quite similar, although the error curve of Adam has, as one would expect from Adam, minor disruptions. Interestingly these disruptions are lining up very well with the disruptions of the change curve of Adam. We found that a DIP reconstruction tends to produce good results, when the choice of the optimizer and its learning rate leads the changes in the null space to be

Table 4.1 Different Reconstructions. Photos for phantoms “4mm” and “2mm” taken at University Medical Center Hamburg-Eppendorf by T. Kluth. For more see Appendix III.

Phantom	Kaczmarz with ℓ_2	ℓ_1	DIP	Photo
“4mm” (DS1)	 $\tilde{\lambda} = 5e-4$	 $\tilde{\lambda} = 5e-3$	 $\eta = 5e-5$	
	 $\tilde{\lambda} = 5e-4$	 $\tilde{\lambda} = 5e-3$	 $\eta = 5e-5$	
“2mm” (DS1)	 $\tilde{\lambda} = 5e-4$	 $\tilde{\lambda} = 5e-3$	 $\eta = 5e-5$	
	 $\tilde{\lambda} = 5e-4$	 $\tilde{\lambda} = 5e-3$	 $\eta = 5e-5$	

roughly on the same order of magnitude as the changes in the orthogonal of the null space. This is the case for our two DIP examples in the table. For the normal Landweber method we used the L-curve to decide when to stop the optimization. We also present the L-curves for the DIP reconstructions. In the DIP with gradient descent reconstruction starts to stagnate in the upper left corner and we could not observe any “exploding” behavior. For DIP with Adam one can see that the L-curve starts the form a “blob”. In our experiments we saw this blob slightly further extending upward if one used further iterations. The visually best results were usually reached shortly after the “blob”-formation started (in this case for example at ca. 100 iterations). The Table 4.2 also presents the “errors per singular value”. We show them since one often uses so called filter functions [10], defined on the singular values, to describe the properties of regularization methods for linear inverse problems. These filter functions specify how the regularization methods deal differently with the minimization of the errors associated with different singular values – more precisely with the different one dimensional subspaces spanned by the singular vectors. We would like to point out that one can see that the DIP reconstructions, allow for much bigger errors in subspaces associated with large singular values. This hints at the DIP being influential in these subspaces, since for the plain Landweber approach one can clearly see a flat region of small errors for the big singular values at later stages of the optimization.

5 Summary and conclusion

In this paper we investigated the concept of deep inverse priors / regularization by architecture. To our knowledge this is the only deep learning method to solve inverse problems that does not require massive amounts of data, which one usually can only acquire after the inverse problem is solved

already. In fact, the method requires one measurement only. We started out by giving different qualitative interpretations of what a regularization is and specifically how regularization by architecture fits into this context.

We followed up with the introduction of the analytic deep inverse prior by specifically showing how proximate gradient descent based architectures, not unlike LISTA, allow for a somewhat transparent regularization by architecture. Specifically we showed that their results can be interpreted as solutions of optimized Tikhonov functionals. This was further investigated with an academic example, where we implemented the analytic deep inverse prior and tested its numerical applicability. The results confirmed our mathematical findings and showed some promising results.

To conclude we applied a deep image prior to the real world problem of computing reconstructions in magnetic particle imaging. We found that this type of regularization compares very well to established and widely used regularization methods, in some cases even surpasses them.

There is obviously, like in deep learning in general, still much work to be done in order to have a good understanding of deep inverse priors, but we see much potential in the idea to use deep architectures to regularize inverse problems; especially since an enormous part of the deep learning research is concerned with the understanding of deep architectures already.

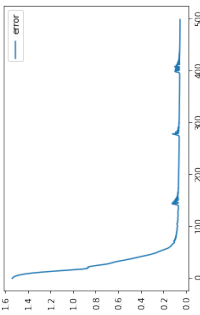
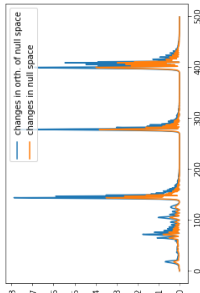
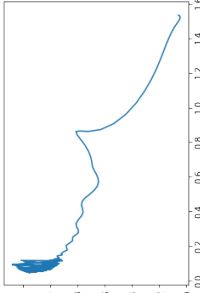
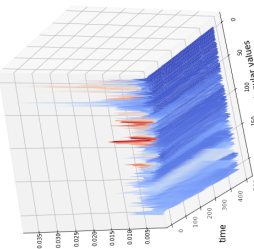
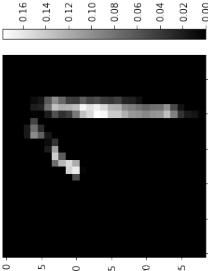
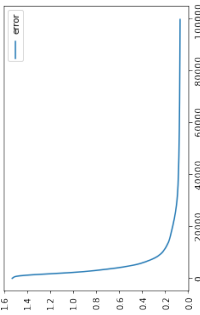
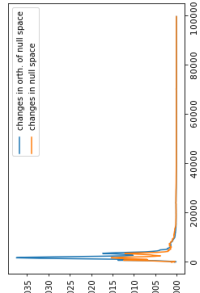
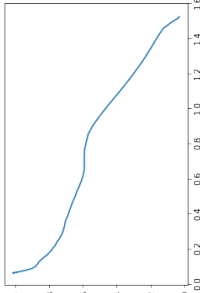
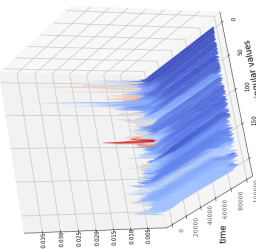
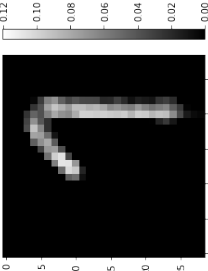
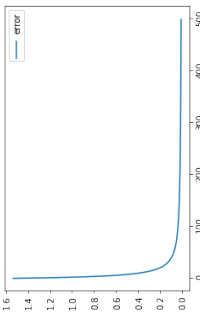
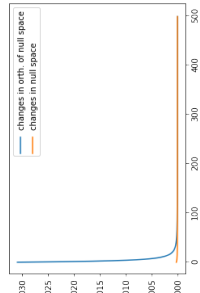
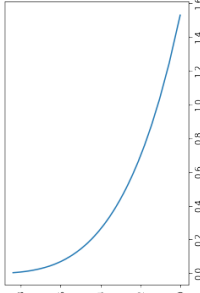
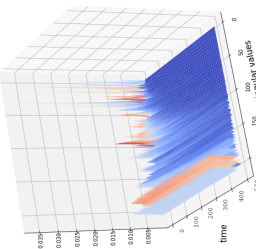
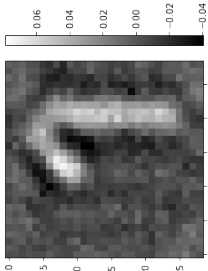
Acknowledgements The authors would like to thank P. Szwarzgulski and T. Knopp from the University Medical Center Hamburg-Eppendorf for their support in conducting the experiments for the dataset DS1.

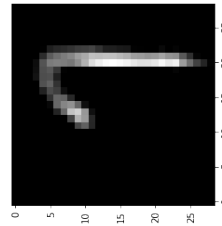
S. Dittmer and T. Kluth acknowledge the support by the Deutsche Forschungsgemeinschaft (DFG) within the framework of GRK 2224/1 “Pi 3 : Parameter IdentificationAnalysis, Algorithms, Applications”.

D. Otero Bager acknowledges the financial support by the Deutsche Forschungsgemeinschaft (DFG, German Research Foundation) - Projektnummer 276397488 - SFB 1232, sub-project “P02-Heuristic, Statistical and Analytical Experimental Design”.

Peter Maass acknowledges funding by the European Union’s Horizon 2020 research and innovation programme under the Marie Sklo-

Table 4.2 Different Reconstruction Methods. Photo for phantom “one” taken at University Medical Center Hamburg-Eppendorf by T. Kluth.

Method	Error	Change	L-curve	Errors per Singular Value	Final Reconstruction
DIP with Adam					
DIP with gradient descent					
Plain Landweber					



Best Adam reconstruction, after 100 iterations.

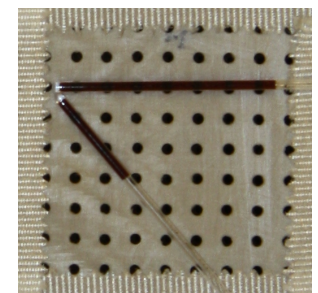


Photo of phantom “one”.

dowska-Curie Grant Agreement No. 765374, sub-project 'Data driven model adaptations of coil sensitivities in MR systems'.

References

- Abadi, M., Agarwal, A., Barham, P., Brevdo, E., Chen, Z., Citro, C., Corrado, G.S., Davis, A., Dean, J., Devin, M., Ghemawat, S., Goodfellow, I., Harp, A., Irving, G., Isard, M., Jia, Y., Jozefowicz, R., Kaiser, L., Kudlur, M., Levenberg, J., Mané, D., Monga, R., Moore, S., Murray, D., Olah, C., Schuster, M., Shlens, J., Steiner, B., Sutskever, I., Talwar, K., Tucker, P., Vanhoucke, V., Vasudevan, V., Viégas, F., Vinyals, O., Warden, P., Wattenberg, M., Wicke, M., Yu, Y., Zheng, X.: TensorFlow: Large-scale machine learning on heterogeneous systems (2015). URL <https://www.tensorflow.org/>.
- Adler, J., Öktem, O.: Learned primal-dual reconstruction. *IEEE transactions on medical imaging* **37**(6), 1322–1332 (2018)
- Anonymous: On the spectral bias of neural networks. In: Submitted to International Conference on Learning Representations (2019). URL <https://openreview.net/forum?id=r1gR2sC9FX>. Under review
- Bathke, C., Kluth, T., Brandt, C., Maass, P.: Improved image reconstruction in magnetic particle imaging using structural a priori information. *International Journal on Magnetic Particle Imaging* **3**(1), ID 1703015, 10 pages (2017). URL <https://journal.iwmpi.org/index.php/iwmpi/article/view/64>
- Beck, A., Teboulle, M.: A fast iterative shrinkage-thresholding algorithm for linear inverse problems. *SIAM Journal on Imaging Sciences* **2**(1), 183–202 (2009). DOI 10.1137/080716542. URL <https://doi.org/10.1137/080716542>
- Bora, A., Jalal, A., Price, E., Dimakis, A.G.: Compressed sensing using generative models. In: Proceedings of the 34th International Conference on Machine Learning, ICML 2017, Sydney, NSW, Australia, 6-11 August 2017, pp. 537–546 (2017). URL <http://proceedings.mlr.press/v70/bora17a.html>
- Chollet, F., et al.: Keras. <https://keras.io> (2015)
- Combettes, P., Wajs, V.: Signal recovery by proximal forward-backward splitting. *Multiscale Modeling & Simulation* **4**(4), 1168–1200 (2005). DOI 10.1137/050626090
- Dax, A.: On row relaxation methods for large constrained least squares problems. *SIAM Journal on Scientific Computing* **14**(3), 570–584 (1993)
- Engl, H.W., Hanke, M., Neubauer, A.: Regularization of inverse problems, *Mathematics and its Applications*, vol. 375. Kluwer Academic Publishers Group, Dordrecht (1996)
- Erb, W., Weinmann, A., Ahlborg, M., Brandt, C., Bringout, G., Buzug, T.M., Frikel, J., Kaethner, C., Knopp, T., März, T., M, M., Storath, M., Weber, A.: Mathematical analysis of the 1D model and reconstruction schemes for magnetic particle imaging. *Inverse Problems* **34**(5), 055012, 21 pp. (2018)
- Franke, J., Heinen, U., Lehr, H., Weber, A., Jaspard, F., Ruhm, W., Heidenreich, M., Schulz, V.: System characterization of a highly integrated preclinical hybrid mpi-mri scanner. *IEEE Transactions on Medical Imaging* **35**(9), 1993–2004 (2016). DOI 10.1109/TMI.2016.2542041
- Franke, J., Lacroix, R., Lehr, H., Heidenreich, M., Heinen, U., Schulz, V.: Mpi flow analysis toolbox exploiting pulsed tracer information an aneurysm phantom proof. *International Journal on Magnetic Particle Imaging* **3**(1) (2017). URL <https://journal.iwmpi.org/index.php/iwmpi/article/view/36>
- Gleich, B., Weizenecker, J.: Tomographic imaging using the nonlinear response of magnetic particles. *Nature* **435**(7046), 1214–1217 (2005)
- Gregor, K., LeCun, Y.: Learning fast approximations of sparse coding. In: ICML 2010 - Proceedings, 27th International Conference on Machine Learning, pp. 399–406 (2010)
- Haegeler, J., Rahmer, J., Gleich, B., Borgert, J., Wojtczyk, H., Panagiotopoulos, N., Buzug, T., Barkhausen, J., Vogt, F.: Magnetic particle imaging: visualization of instruments for cardiovascular intervention. *Radiology* **265**(3), 933–938 (2012)
- Hammernik, K., Klatzer, T., Kobler, E., Recht, M.P., Sodickson, D.K., Pock, T., Knoll, F.: Learning a variational network for reconstruction of accelerated mri data. *Magnetic resonance in medicine* **79**(6), 3055–3071 (2018)
- Hansen, P., OLeary, D.: The use of the l-curve in the regularization of discrete ill-posed problems. *SIAM Journal on Scientific Computing* **14**(6), 1487–1503 (1993)
- Hauptmann, A., Lucka, F., Betcke, M., Huynh, N., Adler, J., Cox, B., Beard, P., Ourselin, S., Arridge, S.: Model-based learning for accelerated, limited-view 3-d photoacoustic tomography. *IEEE transactions on medical imaging* **37**(6), 1382–1393 (2018)
- Jin, K.H., McCann, M.T., Froustey, E., Unser, M.: Deep convolutional neural network for inverse problems in imaging. *IEEE Transactions on Image Processing* **26**(9), 4509–4522 (2017)
- Khandhar, A., Keselman, P., Kemp, S., Ferguson, R., Goodwill, P., Conolly, S., Krishnan, K.: Evaluation of peg-coated iron oxide nanoparticles as blood pool tracers for preclinical magnetic particle imaging. *Nanoscale* **9**(3), 1299–1306 (2017)
- Kingma, D.P., Ba, J.: Adam: A method for stochastic optimization. arXiv preprint arXiv:1412.6980 (2014)
- Kluth, T.: Mathematical models for magnetic particle imaging. *Inverse Problems* **34**(8), 083001 (2018). URL <http://iopscience.iop.org/article/10.1088/1361-6420/aac535>
- Kluth, T., Jin, B., Li, G.: On the degree of ill-posedness of multi-dimensional magnetic particle imaging. *Inverse Problems* **34**(9), 095006 (2018). URL <http://stacks.iop.org/0266-5611/34/i=9/a=095006>
- Kluth, T., Maass, P.: Model uncertainty in magnetic particle imaging: Nonlinear problem formulation and model-based sparse reconstruction. *International Journal on Magnetic Particle Imaging* **3**(2), ID 1707004, 10 pages (2017). URL <https://journal.iwmpi.org/index.php/iwmpi/article/view/74>
- Knopp, T.: Github mdf. <https://github.com/MagneticParticleImaging/MDF>. Accessed: 2018-11-16
- Knopp, T.: Open mpi data. <https://magneticparticleimaging.github.io/OpenMPIData.jl/latest/index.html>. Accessed: 2018-11-16
- Knopp, T., Buzug, T.M.: Magnetic Particle Imaging: An Introduction to Imaging Principles and Scanner Instrumentation. Springer, Berlin/Heidelberg (2012)
- Knopp, T., Gdaniec, N., Möddel, M.: Magnetic particle imaging: from proof of principle to preclinical applications. *Physics in Medicine and Biology* **62**(14), R124 (2017)
- Knopp, T., Hofmann, M.: Online reconstruction of 3D magnetic particle imaging data. *Physics in Medicine and Biology* **61**(11), N257–67 (2016). DOI 10.1088/0031-9155/61/11/N257
- Knopp, T., Rahmer, J., Sattel, T.F., Biederer, S., Weizenecker, J., Gleich, B., Borgert, J., Buzug, T.M.: Weighted iterative reconstruction for magnetic particle imaging. *Phys. Med. Biol.* **55**(6), 1577–1589 (2010)
- Knopp, T., Viereck, T., Bringout, G., Ahlborg, M., von Gladiss, A., Kaethner, C., Neumann, A., Vogel, P., Rahmer, J., Möddel, M.: Mdf: Magnetic particle imaging data format. *ArXiv e-prints* **1602.06072v6**, 1–15 (2018). URL <http://arxiv.org/abs/1602.06072v6>. Article, MDF
- Konkle, J., Goodwill, P., Hensley, D., Orendorff, R., Lustig, M., Conolly, S.: A convex formulation for magnetic particle imaging x-space reconstruction. *PLoS ONE* **10**(10), e0140137 (2015)
- Krizhevsky, A., Hinton, G.: Learning multiple layers of features from tiny images. *Tech. rep., Citeseer* (2009)
- Krizhevsky, A., Sutskever, I., Hinton, G.E.: Imagenet classification with deep convolutional neural networks. In: *Advances in neural information processing systems*, pp. 1097–1105 (2012)

36. Lampe, J., Bassoy, C., Rahmer, J., Weizenecker, J., Voss, H., Gleich, B., Borgert, J.: Fast reconstruction in magnetic particle imaging. *Physics in Medicine and Biology* **57**(4), 1113–1134 (2012). DOI 10.1088/0031-9155/57/4/1113
37. Louis, A.K.: *Inverse und schlecht gestellte Probleme*. Vieweg+Teubner Verlag, Wiesbaden (1989)
38. Maass, P.: Simple networks for trivial inverse problems. submitted for publication (2018)
39. März, T., Weinmann, A.: Model-based reconstruction for magnetic particle imaging in 2D and 3D. *Inv. Probl. Imag.* **10**(4), 1087–1110 (2016)
40. Meinhardt, T., Möller, M., Hazirbas, C., Cremers, D.: Learning proximal operators: Using denoising networks for regularizing inverse imaging problems. In: *IEEE International Conference on Computer Vision*, pp. 1781–1790 (2017)
41. Murase, K., Aoki, M., Banura, N., Nishimoto, K., Mimura, A., Kuboyabu, T., Yabata, I.: Usefulness of magnetic particle imaging for predicting the therapeutic effect of magnetic hyperthermia. *Open Journal of Medical Imaging* **5**(02), 85 (2015)
42. Nesterov, Y.: *Lectures on Convex Optimization*. Springer Optimization and Its Applications. Springer International Publishing (2019). URL <https://books.google.de/books?id=JSyNtQEACAAJ>
43. Rahmer, J., Weizenecker, J., Gleich, B., Borgert, J.: Analysis of a 3-D system function measured for magnetic particle imaging. *IEEE Transactions on Medical Imaging* **31**(6), 1289–1299 (2012)
44. Rieder, A.: *Keine Probleme mit inversen Problemen: eine Einführung in ihre stabile Lösung*. Vieweg, Wiesbaden (2003)
45. Salamon, J., Hofmann, M., Jung, C., Kaul, M.G., Werner, F., Them, K., Reimer, R., Nielsen, P., vom Scheidt, A., Adam, G., Knopp, T., Ittrich, H.: Magnetic particle/magnetic resonance imaging: In-vitro MPI-guided real time catheter tracking and 4D angioplasty using a road map and blood pool tracer approach. *PLoS ONE* **11**(6), e0156899–14 (2016)
46. Saxe, A.M., McClelland, J.L., Ganguli, S.: Exact solutions to the nonlinear dynamics of learning in deep linear neural networks. arXiv preprint arXiv:1312.6120 (2013)
47. Storath, M., Brandt, C., Hofmann, M., Knopp, T., Salamon, J., Weber, A., Weinmann, A.: Edge preserving and noise reducing reconstruction for magnetic particle imaging. *IEEE Transactions on Medical Imaging* **36**(1), 74–85 (2017). DOI 10.1109/TMI.2016.2593954
48. Szegedy, C., Vanhoucke, V., Ioffe, S., Shlens, J., Wojna, Z.: Rethinking the inception architecture for computer vision. In: *Proceedings of the IEEE conference on computer vision and pattern recognition*, pp. 2818–2826 (2016)
49. Them, K., Kaul, M.G., Jung, C., Hofmann, M., Mummert, T., Werner, F., Knopp, T.: Sensitivity enhancement in magnetic particle imaging by background subtraction. *IEEE Trans. Med. Imag.* **35**(3), 893–900 (2016). DOI 10.1109/TMI.2015.2501462
50. Ulyanov, D., Vedaldi, A., Lempitsky, V.S.: Deep image prior. *CoRR* **abs/1711.10925** (2017). URL <http://arxiv.org/abs/1711.10925>
51. Van Veen, D., Jalal, A., Price, E., Vishwanath, S., Dimakis, A.G.: Compressed sensing with deep image prior and learned regularization. arXiv preprint arXiv:1806.06438 (2018)
52. Vonesch, C., Unser, M.: A fast iterative thresholding algorithm for wavelet-regularized deconvolution - art. no. 67010d. *Wavelets XII, Pts 1 And 2* **6701**, D7010–D7010 (2007)
53. Weizenecker, J., Gleich, B., Rahmer, J., Dahnke, H., Borgert, J.: Three-dimensional real-time in vivo magnetic particle imaging. *Physics in Medicine and Biology* **54**(5), L1 (2009)
54. Yu, E.Y., Bishop, M., Zheng, B., Ferguson, R.M., Khandhar, A.P., Kemp, S.J., Krishnan, K.M., Goodwill, P.W., Conolly, S.M.: Magnetic particle imaging: A novel in vivo imaging platform for cancer detection. *Nano Letters* **17**(3), 1648–1654 (2017). DOI 10.1021/acs.nanolett.6b04865. URL <http://dx.doi.org/10.1021/acs.nanolett.6b04865>
55. Zhang, C., Bengio, S., Hardt, M., Recht, B., Vinyals, O.: Understanding deep learning requires rethinking generalization. arXiv preprint arXiv:1611.03530 (2016)

Appendix I: A reminder on minimization of Tikhonov functionals and the LISTA approach

In this section we consider only linear operators A and we review the well known theory for the Iterative Soft Shrinkage Algorithm (ISTA) as well as the slightly more general Proximal Gradient (PG) [8,42] method for minimizing Tikhonov functionals of the type

$$J(x) = \frac{1}{2} \|Ax - y^\delta\|^2 + \alpha R(x). \quad (5.1)$$

We recapitulate the main steps in deriving ISTA and PG, as far as we need it for our motivation. The necessary first order condition for a minimizer is given by

$$0 \in A^*(Ax - y^\delta) + \alpha \partial R(x). \quad (5.2)$$

Multiplying with an arbitrary real positive number λ and adding x plus rearranging yields

$$x - \lambda A^*(Ax - y^\delta) \in x + \lambda \alpha \partial R(x). \quad (5.3)$$

For convex R , the term of the right hand side is inverted by the (single valued) proximal mapping of $\lambda \alpha R$, which yields

$$\text{Prox}_{\lambda \alpha R} \left(x - \lambda A^*(Ax - y^\delta) \right) = x. \quad (5.4)$$

Hence this is a fixed point condition, which is a necessary condition for all minimizers of J . Turning the fixed point condition into an iteration scheme yields the PG method

$$x^{k+1} = \text{Prox}_{\lambda \alpha R} \left(x^k - \lambda A^*(Ax^k - y^\delta) \right) \quad (5.5)$$

$$= \text{Prox}_{\lambda \alpha R} \left((I - \lambda A^*A)x^k + \lambda A^*y^\delta \right). \quad (5.6)$$

This structure is also the motivation for LISTA [15] approaches where fully connected networks with L internal layers of identical size are used. Moreover, in some versions of LISTA, the affine maps between the layers are assumed to be identical. The values at the k -th layer are denoted by x^k , hence,

$$x^{k+1} = \phi \left(Wx^k + b \right). \quad (5.7)$$

LISTA then trains (W, b) on some given training data. More precisely, it trains two matrices $W = I - \lambda A^*A$ and $S = \lambda A^*$ such that

$$x^{k+1} = \phi \left(Wx^k + Sy^\delta \right). \quad (5.8)$$

This derivation can be rephrased as follows.

Lemma 5.1 Let φ_W denote a fully connected network with input x^0 and L -internal layers. Further assume, that the activation function is identical to a proximal mapping for a convex functional $\lambda\alpha R : X \rightarrow \mathbb{R}$. Assume W is restricted, such that $I - W$ is positive definite, i.e. there exists a matrix B such that

$$I - W = \lambda B^* B. \quad (5.9)$$

Furthermore, we assume that the bias term is fixed as $b = \lambda B^* y^\delta$. Then $\varphi_W(z)$ is the L -th iterate of an ISTA scheme with starting value $x^0 = z$ for minimizing

$$J_B(x) = \frac{1}{2} \|Bx - y^\delta\|^2 + \alpha R(x). \quad (5.10)$$

Proof Follows directly from equation (5.5).

Following these arguments one can rephrase LISTA as a concept for learning the discrepancy term in a classical Tikhonov functional. This point of view opens further connections to variational approaches in deep learning, see e.g. [17, 40]

Appendix II: Numerical experiments

In this section we provide details about the implementation of the analytic deep inverse prior and the academic example.

Discretizing the integration operator yields the matrix $A_n \in \mathbb{R}^{n \times n}$, which has $\frac{h}{2}$ on the main diagonal, h everywhere under the main diagonal and 0 above (here $h = \frac{1}{n}$). In our experiments we use $n = 200$.

The analytic deep inverse prior network is implemented using Python and Tensorflow [1]. Initially, the weight matrix $B \in \mathbb{R}^{n \times n}$ is created and then L fully connected layers are added to the network, all having the same weight matrix $W = I - \lambda B^T B$, bias $b = \lambda B^T y^\delta$ and activation function given by (3.17). That means the network contains in total 4×10^4 parameters (the number of components in B), independently from the number L of layers. For the experiments shown in the paper the input z is randomly initialized with small norm and λ is $\frac{1}{\mu}$, where μ is the biggest eigenvalue of $A^T A$.

In order to guarantee that assumption (3.4) holds, the network should in principle have thousands of layers, because of the slow convergence of the PG method. However, this is prohibitive from the implementation point of view. During the training iterations, in which we update B , we therefore consider only a reduced network with a small number, $L = 10$, of layers but we set the input to be the network's output after the previous iteration. This is equivalent to adding L new identical layers, with $W_k = I - \lambda B_k^T B_k$ and $b_k = \lambda B_k^T y^\delta$, at the end of an implicit network which is growing by L layers at a time. Here B_k refers to the k -th update of B when applying gradient descent to minimize (1.1).

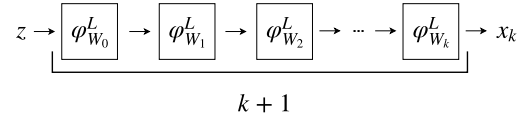


Fig. 5.1 The implicit network with $(k+1)L$ layers. Here $\varphi_{W_k}^L$ refers to a block of L identical fully connected layers with weights $W_k = I - \lambda B_k^T B_k$ and $b_k = \lambda B_k^T y^\delta$.

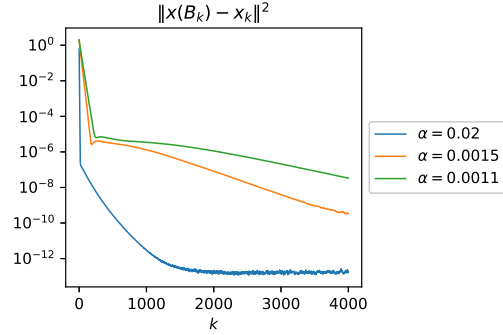


Fig. 5.2 Difference between x_k and $x(B_k)$ after each training iteration k corresponding to the experiments from Figure 3.2.

After the k -th iteration, we have implicitly created a network that has $(k+1)L$ layers. However, in the next iteration B is updated considering only back-propagation over the last L layers.

Let x_k be the output of this implicit network after iteration k , see Figure 5.1. In order to properly update B by the back-propagation, we need x_k to be a good approximation of $x(B_k)$. We checked empirically that $x_k \rightarrow x(B_k)$ when $k \rightarrow \infty$ by evaluating $x(B_k) = (B_k^T B_k + \alpha I)^{-1} B_k^T y^\delta$ and computing $\|x_k - x(B_k)\|^2$ at each iteration. The results are shown in Figure 5.2. As it can be observed, after $k > 100$ the error is considerably low.

For the adaptive choice of α , we set it as a variable in Tensorflow, i.e. at each training iteration α and B are updated by the gradient descent. It is expected from the setup in Def. 3.1 that $\alpha \rightarrow 0$ and this was indeed observed in the experiments, see Figure 3.3. What is interesting is that it first decays fast and then continues to decrease slowly. Moreover, the turning point corresponds to an iteration that is quite close to the optimal one when looking at the true error plot in Figure 3.3. Based on that, we used it as stopping criterion for selecting k^* .

Appendix III: Magnetic particle imaging (MPI)

In this appendix we summarize the state of the art concerning analytic models for MPI and we give a detailed description on the MPI experiments using deep inverse prior networks.

Precisely modeling MPI, resp. formulating a physically accurate integral kernel for image reconstruction, is still an unsolved problem. Various modeling aspects, e.g. the magnetization dynamics and particle-particle interactions make it a challenging task such that the integral kernel is commonly determined in a time-consuming calibration procedure. For further information on the modeling aspects the interested reader is referred to the survey paper [24] as well as to the review article [29] for further details on the MPI methodology.

A first step towards a theoretical understanding of this problem, while excluding the temporal dependence, can be found in [39]. A one-dimensional problem setup considering the time-dependency of the measurements was analyzed in [11] for one particular trigonometric excitation. Furthermore, the multi-dimensional imaging problem for different dynamic magnetic field patterns was analyzed in the context of inverse problems regarding the best possible degree of ill-posedness [23]. The theoretical investigations so far (based on the simplified equilibrium model [24]) conclude that in the MPI standard setup, which uses a superposition of trigonometric dynamic field excitations and linear gradient fields, is severely ill-posed.

The concentration reconstruction problem is typically solved by applying Tikhonov regularization [31, 36, 43, 53]. For MPI this is preferably solved by using the algebraic reconstruction technique [30, 31] combined with a non-negativity constraint [53]. More recently, further sophisticated regularization techniques such as fused lasso regularization, directional total variation, or other gradient-based methods have been applied to the full-calibration-based MPI problem [4, 33, 47]. A total-least-squares approach with respect to operator uncertainty combined with standard Tikhonov regularization as well as a sparsity-promoting penalty term was used to improve reconstruction performance [25].

5.1 How Magnetic Particle Imaging works

For the description of the MPI setup we adapt the general notations in [23, 24]. MPI is inherently a 3D problem such that vector-valued functions remain 3D even if the domain Ω of the spatial variable x is a subset of a d -dimensional affine subspace $E_d \subset \mathbb{R}^3$. It is further assumed that the support of the concentration function is a subset of the domain Ω . A lower dimensional setup ($d < 3$) can be constructed by the assumption that the concentration is a δ -distribution with respect to the orthogonal complement of E_d . Let $\Omega \subset E_d$, $d = 1, 2, 3$, be a bounded domain with a (strong) Lipschitz boundary $\partial\Omega$ in E_d . Further, let $T > 0$ denote the maximal data acquisition time and $I := (0, T)$ the time interval during which the measurement process takes place. The temporal derivative of any function $g : I \rightarrow \mathbb{R}^d$ is denoted by \dot{g} .

The measured voltage signal $v_\ell : I \rightarrow \mathbb{R}$, $\ell = 1, \dots, L$, obtained at $L \in \mathbb{N}$ receive coils, is given by

$$v_\ell(t) = \int_{\Omega} c(x) \underbrace{\int_I -a_\ell(t-t') \mu_0 p_\ell(x)^t \dot{\bar{m}}(x,t) dt'}_{=s_\ell(x,t)} dx - \underbrace{\int_I \int_{\mathbb{R}^3} a_\ell(t-t') \mu_0 p_\ell(x)^t \dot{H}(x,t) dx dt'}_{=v_{E,\ell}(t)}, \quad (5.11)$$

where the superscript t denotes the transpose of a vector, $c : \Omega \rightarrow \mathbb{R}^+ \cup \{0\}$ is the concentration of the magnetic nanoparticles and $s_\ell : \Omega \times I \rightarrow \mathbb{R}$, $\ell = 1, \dots, L$, represent the system functions characterizing the mean magnetic moment behavior $\bar{m} : \Omega \times I \rightarrow \mathbb{R}^3$ of nanoparticles. This relation follows from Faraday's law and the law of reciprocity [28]. The positive constant μ_0 is magnetic permeability in vacuum. The scalar functions $a_\ell : \bar{I} := [-T : T] \rightarrow \mathbb{R}$, $\ell = 1, \dots, L$, are the analog filters in the signal acquisition chain, and in practice, they are commonly band stop filters adapted to excitation frequencies of the drive field. Note that the analog filters a_ℓ are included in the system functions in this formulation, which can differ in the literature. The functions $p_\ell : \mathbb{R}^3 \rightarrow \mathbb{R}^3$, $\ell = 1, \dots, L$, denote the sensitivity profiles of the receive coil units.

In the following it is assumed that the applied magnetic field $H : \mathbb{R}^3 \times I \rightarrow \mathbb{R}^3$ and the filters $\{a_\ell\}_{\ell=1}^L$ are chosen in a way such that all excitation signals $v_{E,\ell} = 0$, $\ell = 1, \dots, L$. This assumption on the excitation signals $\{v_{E,\ell}\}_{\ell=1}^L$ is commonly made but may not be fulfilled in MPI applications [25, 49]. Using the previous assumption the inverse problem is to find the concentration $c : \Omega \rightarrow \mathbb{R}^+ \cup \{0\}$ from $\{v_\ell\}_{\ell=1}^L$:

$$v_\ell(t) = \int_{\Omega} c(x) s_\ell(x,t) dx = S_\ell c(t), \quad (5.12)$$

where $S_\ell : L^2(\Omega) \rightarrow L^2(I)$.

We can now distinguish two cases in MPI regarding a formal description of the forward operator, the *data-based* case where a full calibration of the linear forward operator is performed and the *model-based* case where a suitable model for the mean magnetic moment \bar{m} is formulated. Due to the fact that finding a suitable model for the particles' magnetization is still an unsolved problem and the full system matrix calibration is still state of the art in MPI, we restrict the application of the Deep Image prior to the data-based case, which uses a small tracer sample as follows: Let $\Gamma \subset \mathbb{R}^3$ be a reference volume placed at the origin. The data-based approach uses single measurements of a small sample at predefined positions $\{x^{(i)}\}_{i=1,\dots,N} \in \Omega^N$. The concentration phantoms are given by $c^{(i)} = c_0 \chi_{x^{(i)} + \Gamma}$ for some reference concentration $c_0 > 0$. Typical choices for Γ are small cubes. The measurements $v_\ell^{(i)} = \frac{1}{c_0} S_\ell c^{(i)}$, $i = 1, \dots, N$, are then used to

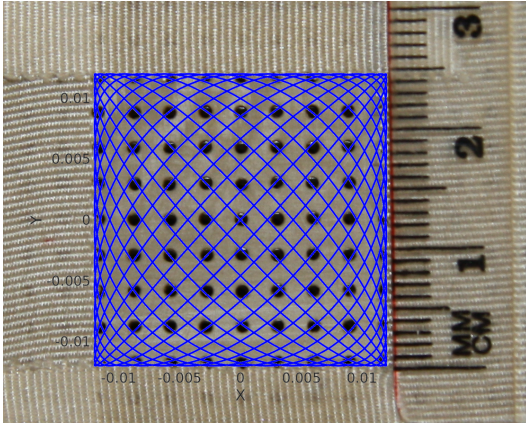


Fig. 5.3 Experimental platform used to obtain dataset DS1 with FFP Lissajous trajectory in blue. Photo taken at University Medical Center Hamburg-Eppendorf by T. Kluth.

characterize the discrete data-based forward operator via a system matrix ($L = 3$)

$$S = \begin{bmatrix} (\langle v_1^{(i)}, \Psi_j \rangle)_{j \in J_1, i=1, \dots, N} \\ (\langle v_2^{(i)}, \Psi_j \rangle)_{j \in J_2, i=1, \dots, N} \\ (\langle v_3^{(i)}, \Psi_j \rangle)_{j \in J_3, i=1, \dots, N} \end{bmatrix}, \quad (5.13)$$

where $\{\Psi_j\}_{j \in \mathbb{Z}}$ is the Fourier basis of time-periodic signals of $L^2(I)$, i.e. $\Psi_j(t) = 1/\sqrt{T}(-1)^j e^{i2\pi jt/T}$, $j \in \mathbb{Z}$. $J_\ell \subset \mathbb{Z}$, $\ell = 1, 2, 3$, are restrictions to index sets for the purpose of a preprocessing prior the reconstruction. For given phantom measurements v_ℓ , $\ell = 1, 2, 3$, we build the measurement vector analogously, i.e.,

$$v = \begin{bmatrix} (\langle v_1, \Psi_j \rangle)_{j \in J_1} \\ (\langle v_2, \Psi_j \rangle)_{j \in J_2} \\ (\langle v_3, \Psi_j \rangle)_{j \in J_3} \end{bmatrix}. \quad (5.14)$$

5.2 Experimental setup

We test the capability of the deep imaging prior approach to improve image reconstruction. This is done by using two datasets generated by using the Bruker preclinical MPI system at the University Medical Center Hamburg-Eppendorf. A 2D excitation in the x/y-direction is used with excitation frequencies of 2.5/102 MHz (≈ 24.51 kHz) and 2.5/96 MHz (≈ 26.04 kHz) resulting in a 2D Lissajous trajectory with a period of approximately 0.6528 ms. The drive field amplitude in x- and y-direction is 12 mT/ μ_0 respectively. The gradient strength of the selection field is 2 T/m/ μ_0 in z-direction and -1 T/m/ μ_0 in x- and y-direction. The time-dependent voltage signal is sampled with a rate of 2.5 MHz from $L = 3$ receive coil units. The discretization in time and the real-valued signal results in 817 available Fourier coefficients (for Ψ_j , $j \in \{0, \dots, 816\}$) for each receive coil. Thus each system matrix S has at most $3 \cdot 817 = 2451$ rows. The two datasets are as follows:

DS1 2D phantom dataset: The system matrix is obtained by using a cubic sample with edge length of 1 mm. The calibration is done with Resovist[®] tracer with a concentration of 0.25 mol/l. The field-of-view has a size of 29 mm \times 29 mm \times 3 mm and the sample positions have a distance of 1 mm in each direction resulting in a size of 29 \times 29 \times 3 voxels, i.e., 2523 columns in the system matrix. System matrix entries are averaged over 200 repetitions and empty scanner measurements are performed every 29 calibration scans. It is ensured that the used phantoms are positioned within the calibrated FOV by moving an experimental platform in the desired region, see Figure 5.3. The phantom measurements are averaged over 10,000 repetitions of the excitation sequence. We use the three following phantoms:

- “4mm”: Two cylindrical glass capillary with an inner diameter of 0.7 mm filled with Resovist[®] with a concentration of 0.25 mol/l are placed in the x/y-plane oriented in y-direction. The heights of the tracer in the capillaries are 10 mm (left capillary) and 21 mm (right capillary). The distance between the capillaries in x-direction is 4 mm. See also Table 5.1 for an illustration.
- “2mm”: Like the “4mm” phantom with 2 mm distance in x-direction between the glass capillary. See also Table 5.1 for an illustration.
- “one”: The same capillaries from the “4mm” phantom are used and arranged as the digit one. See also Table 4.2 for an illustration.

DS2 Open MPI dataset: The dataset is publicly available at [27]. From the dataset the 2D calibration system matrix for the x/y-plane located at z=0 mm is used for the reconstruction. Here, the system matrix is obtained by using a cuboid sample with an edge length of 2 mm \times 2 mm \times 1 mm. The calibration is done with Perimag[®] tracer with a concentration of 0.1 mol/l. The considered field-of-view has a size of 38 mm \times 38 mm \times 1 mm and the sample positions have a distance of 2 mm in x- and y-direction resulting in a size of 19 \times 19 \times 1 voxels, i.e., 361 columns in the system matrix. System matrix entries are averaged over 1000 repetitions and empty scanner measurements are performed every 19 calibration scans. In contrast to the previous dataset the used phantoms are not limited to the covered field of view of the system matrix. The phantom measurements are averaged over 1000 repetitions of the excitation sequence. According to the description on [27] we have the following three phantoms:

- “concentration”: This phantom consists of 8 cubes of 2mm edge length resulting in 8 μ l volume each. The distance of the cubes is 12 mm between centers (10 mm between edges) within the x/y-plane and 6 mm between centers (4 mm between edges) in z-

direction. The sample chambers are numbered from 1 to 8 starting with the top layer on the top left position (positive x- and y-direction), counting clockwise. Then starting with the lower layer with number 5 on the top left (positive X and Y direction), counting clockwise. The concentrations in the 8 sample chambers are diluted with a factor of 1.5 in each step and the values are 100.0, 66.6, 44.4, 29.6, 19.7, 13.1, 8.77, and 5.85 mmol/l. See also Table 5.1 for an illustration.

- “*shape*”: The phantom is a cone defined by a 1 mm radius tip, an apex angle of 10 deg, and a height of 22 mm. The total volume is 683.9 μL . Perimag[®] tracer with a concentration of 0.05 mol/L is used. See also Table 5.1 for an illustration.
- “*resolution*”: The resolution phantom consists of 5 tubes filled with Perimag[®] with a concentration of 0.05 mol/l. The 5 tubes have a common origin on one side of the phantom. From there they extend in different angles from this origin within the x/y- and the y/z-plane. In z-direction the angles in the y/z-plane are chosen smaller (10 deg and 15 deg) than in x/y-plane (20 deg and 30 deg). See also Table 5.1 for an illustration.

All data is provided in the Magnetic Particle Imaging Data Format Files (MDF) encoded according to [26, 32].

5.3 Preprocessing, network and training

In MPI there exist two standard preprocessing approaches which are commonly combined via the index sets J_ℓ , $\ell = 1, 2, 3$: A band pass approach and an SNR-type thresholding. Let $I_{\text{BP}} = \{j \in \mathbb{Z} \mid b_1 \leq |j|/T \leq b_2\}$ be the band pass indices for frequency band limits $0 \leq b_1 < b_2 \leq \infty$. For the SNR-type thresholding one standard quality measure is determined by computing a ratio of mean absolute values from individual measurements $v_\ell^{(i)}$ (as previously described) and a set of empty scanner measurements $\{v_{\ell,0}^{(k)}\}_{k=1}^K$ [12]:

$$d_{\ell,j} = \frac{\frac{1}{N} \sum_{i=1}^N |\langle v_\ell^{(i)} - \mu_\ell^{(i)}, \psi_j \rangle|}{\frac{1}{K} \sum_{k=1}^K |\langle v_{\ell,0}^{(k)} - \mu_\ell, \psi_j \rangle|} \quad (5.15)$$

where $\mu_\ell = \frac{1}{K} \sum_{k=1}^K v_{\ell,0}^{(k)}$ and $\mu_\ell^{(i)} = \kappa_i v_{\ell,0}^{(k_i)} + (1 - \kappa_i) v_{\ell,0}^{(k_i+1)}$ is a convex combination of the previous (k_i -th) and following ($k_i + 1$ -th) empty scanner measurement with respect to the i -th calibration scan; the parameters $\kappa_i \in [0, 1]$ are chosen equidistant for all calibration scans between two subsequent empty scanner measurements. For a given threshold $\tau \geq 0$ we thus obtain

$$J_\ell = \{j \in I_{\text{BP}} \mid d_{\ell,j} \geq \tau\} \quad (5.16)$$

for $\ell = 1, 2, 3$.

We will now describe the general setup we use to apply the deep inversion prior approach to the reconstruction of 2 dimensional magnetic particle imaging data.

We do the **preprocessing** of the data in the following manner:

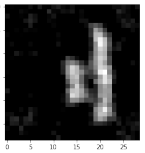
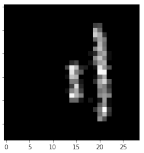
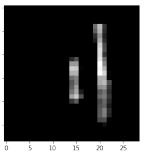
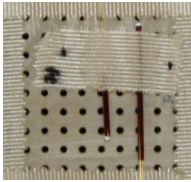
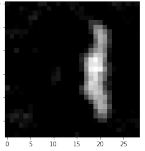
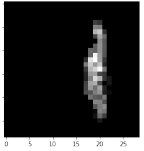
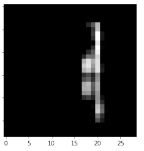
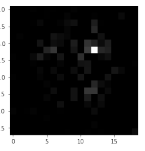
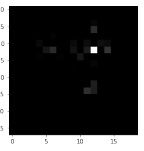
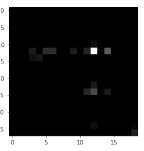
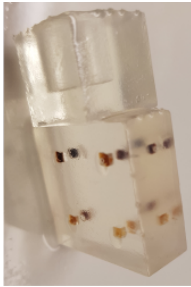
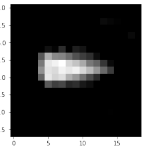
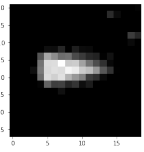
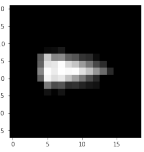
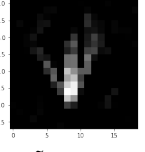
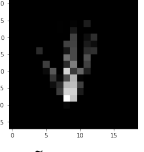
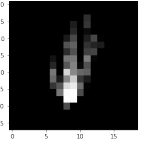
1. We build the system matrix S and the measurement v (represented as described in (5.13) and (5.14)) which are associated with the index sets J_ℓ , $\ell = 1, 2, 3$, based on an SNR-type thresholding with $\tau = 2$ ($(d_{\ell,j})_{j \in J_\ell}$ also provided by the MDF file) and the bandpass index set with the passband boundaries $b_1 = 80$ kHz and $b_2 = 625$ kHz.
2. We subtract the signal of an empty scanner measurement analogously represented as in (5.14) by v_0 from the phantom data to correct for the background signal.
3. The resulting linear equation system $Sc = v$ is multiplied with a diagonal matrix W with the reciprocal of the 2-norm of the respective row of the system matrix on the diagonal.

This leaves us with the a processed system matrix, to which we will from now on refer to as $A = WS \in \mathbb{C}^{M \times N}$, and signals to which we will from now on refer to as $y^\delta = W(v - v_0) \in \mathbb{C}^M$, $M = \sum_{\ell=1}^L |J_\ell|$. For DS1 we end up with $M = 211$ and $N = 29^2 \cdot 3 = 2523$ and for DS2 with $M = 842$ and $N = 19^2 = 361$.

We will now describe the **network** we are using to deploy our deep image prior / regularization by architecture approach to magnetic particle imaging as described above. Since it is not clear what a good prior for MPI is or how one would encode one would cast it into a regularizing architecture. Here, we use the deep image prior introduced by [50], specifically their U-net architecture. Our implementation is based on Tensorflow [1] and Keras [7] and has the following specifications: Between the encoder and decoder part of the U-net our skip connection have 4 channels. The convolutional encoder goes from the input to 32, 32, 64 and 128 channels each with strides of 2×2 and filters of size 3×3 . Then the convolutional decoder has the mirrored architecture (i.e. “up-sampling” strides and 128, 64, 32, 32 channels) plus first a resize-nearest-neighbor layer to reach the desired output shape, second an additional ReLU convolutional layer with filters of size 1 and third a scaling factor, $1e - 2$, to accommodate the scale of the reconstruction. The number of channels of this last layers is 3 for data set 1 (DS1) (three 2-dimensional scans above one another) of a 2-dimensional phantom centered at the central slice of the three. The input of the network is given by a fixed Gaussian random input of size $3 \times 32 \times 32$. For further details on this architecture we refer to [50]

Sometimes our optimization apparently got stuck in an undesirable local minimum early on. In those cases we simply restarted the optimization (with a new random initialization of the network).

Table 5.1 An extended version of Figure 4.1. Different Reconstructions. Photos for phantoms “4mm” and “2mm” taken at University Medical Center Hamburg-Eppendorf by T. Kluth. Photos for phantoms “concentration”, “shape”, and “resolution” as provided by [27].

Phantom	Kaczmarz with ℓ_2	ℓ_1	DIP	Photo
“4mm” (DS1)	 $\tilde{\lambda} = 5e-4$	 $\tilde{\lambda} = 5e-3$	 $\eta = 5e-5$	
	 $\tilde{\lambda} = 5e-4$	 $\tilde{\lambda} = 5e-3$	 $\eta = 5e-5$	
“concentration” (DS2)	 $\tilde{\lambda} = 5e-3$	 $\tilde{\lambda} = 1e-2$	 $\eta = 5e-5$	
	 $\tilde{\lambda} = 5e-3$	 $\tilde{\lambda} = 1e-2$	 $\eta = 5e-5$	
“shape” (DS2)	 $\tilde{\lambda} = 5e-3$	 $\tilde{\lambda} = 5e-3$	 $\eta = 5e-5$	